Infrared radiation transfer through semitransparent windows supporting absorbing droplets

Eylul Simsek[a], Megan J. Williams[a], Jack Hoeniges[a], Keyong Zhu[b], Laurent Pilon[a,c,d,*]

[a] Mechanical and Aerospace Engineering Department, University of California Los Angeles, Los Angeles, CA 90095-1597, USA
[b] School of Aeronautical Science and Engineering, Beihang University, Beijing 100191, China
[c] California NanoSystems Institute, University of California Los Angeles, Los Angeles, CA 90095, USA
[d] Institute of the Environment and Sustainability, University of California Los Angeles, Los Angeles, CA 90095, USA

ABSTRACT

Water droplets are commonly observed on the inner or outer surface of solar energy conversion systems due to rain or condensation. These droplets affect the systems' efficiency and thermal load. This study experimentally and numerically investigates infrared radiation transfer through semitransparent windows covered with droplets on their front or back sides. In order to validate our previously developed numerical code and to facilitate the systematic characterization of the samples, acrylic droplets (instead of water) were deposited onto glass windows with contact angle ranging from 26 to 76° and projected surface area coverage from 0% to 60%. The measured transmittance of glass windows with slightly absorbing droplets on the front increased while the reflectance decreased with increasing contact angle and surface coverage due to antireflection effects. For slightly absorbing droplets on the back with contact angles larger than the critical angle for total internal reflection at the droplet/air interface, the transmittance decreased by up to a factor 2 with increasing contact angle and surface area coverage. In the infrared spectral range when droplets were strongly absorbing, the window transmittance decreased by up to a factor 2.5 with increasing surface coverage for droplets either on the front or back sides. Experimental measurements were in excellent agreement with numerical predictions obtained using the Monte Carlo ray-tracing method. Then, the experimentally-validated simulation tool was used to predict the solar transmittance and emittance of glass windows covered with water droplets. The solar transmittance was found to decrease significantly with water droplets on either side depending on the time of day while the emittance remained unchanged.

1. Introduction

Water droplets are commonly observed on the inner or outer surface of covers of solar stills [1–7], solar water heaters [8,9], solar photovoltaic panels [10–13], solar collectors [14], greenhouses [15–20], outdoor photobioreactors [21–23], covered raceway ponds [24], and building windows [25–28], as shown in Fig. 1. Water droplets may be present due to rain or as a result of dropwise condensation when the temperature of a surface is lower than the dew point temperature of the surrounding air. In addition, these solar systems have an operating temperature ranging from 280 K to 320 K and emit thermal radiation at infrared wavelengths (4

μm $\leq \lambda \leq$ 40 μm) with a peak emissive power occurring around 10 μm while being exposed, during the day, to solar radiation concentrated in the spectral range 400 nm $\leq \lambda \leq$ 3 μm [29]. The presence of droplets on either side can alter the transmission of solar radiation and the emissivity of the covers and windows, thereby impacting the energy input and the thermal load on the systems.

The interaction between visible light and semitransparent plastic film or window covers supporting non-absorbing droplets has been studied both numerically [24,30–34] and experimentally [16–18,35–38]. The reader is referred to Refs. [32,39] for a more detailed review. In brief, the presence of such droplets has been shown to reduce the transmittance through the plastic covers or windows in the visible (400 nm $\leq \lambda \leq$ 750 nm) and near-infrared (750 nm $< \lambda \leq$ 3 μm) parts of the electromagnetic spectrum thereby decreasing the solar energy input available for photosynthesis [24,35,40–43] or for solar photothermal and photoelectric

* Corresponding author at: Mechanical and Aerospace Engineering Department, University of California Los Angeles, Los Angeles, CA 90095-1597, USA.
E-mail address: pilon@seas.ucla.edu (L. Pilon).

Fig. 1. Water droplets on the surface of (a) a solar still cover (photo by Michael J Scheepers, Design Engineer, Teq Design Central, mickeys@teq-dc.com), (b) a solar photovoltaic panel (credit: photograph reproduced with permission from GÜNAM, http://gunam.metu.edu.tr/), (c) a greenhouse cover (credit: photograph reproduced with permission from ZipGrow Incorporated, www.ZipGrow.com), and of (d) a window.

energy conversions [31,44,45]. This has been attributed to backscattering and/or absorption by droplets [30–32,46,47]. Moreover, the numerical simulations for glass windows supporting droplets on their *back side* have recently been validated experimentally in the visible and near-infrared (0.4–1.1 μm) for acrylic droplets deposited on the back side of 3 mm-thick soda-lime glass slabs with or without hydrophobic coatings corresponding to droplet contact angle θ_c between 26° and 76° and surface area coverage f_A between 19% and 59% [38]. However, to the best of our knowledge, the impact of droplets on infrared radiation transfer through windows has not yet been investigated experimentally.

The objective of this study is to experimentally and numerically investigate infrared radiation transfer through semitransparent glass windows covered with absorbing droplets on either their back or front sides. To do so, glass windows supporting a large number of polydisperse acrylic droplets with different surface area coverages and contact angles were prepared and carefully characterized. For the first time, the spectral normal-hemispherical transmittance and reflectance of the droplet-covered glass windows were measured in the infrared where both the glass window and the droplets were weakly to strongly absorbing. The experimental measurements were used to validate a numerical code based on the Monte Carlo ray-tracing (MCRT) method and the results of previous parametric studies when the droplets and/or the glass windows were absorbing [31,32,46]. Finally, the experimentally-validated numerical code was used to predict the hourly solar transmittance and total hemispherical emittance of the glass windows supporting water droplets on their back or front side. The

results of this study can be used to optimize the thermal management and performance of buildings and solar energy conversion systems affected by the presence of water droplets.

2. Materials and methods

2.1. Samples

The same samples as those prepared and described in detail in our previous study [38] were used in the present study to validate experimentally the numerical code in the infrared part of the spectrum. In brief, all samples consisted of 3 mm-thick plane-parallel soda-lime glass slabs (Asahi Glass Corporation, Yokohama, Japan) with a surface area of 2.5 × 2.5 cm^2. Nine different samples with or without hydrophobic coatings were prepared. Once the uncoated or coated glass slabs were prepared, droplets made of acrylic polymer (Loctite AA 349) were deposited onto the glass and cured with a UV lamp (Blak-Ray B-100A, Thermo Scientific Fisher, USA) emitting at a wavelength 365 nm. Polymer droplets were used instead of water droplets to avoid changes in the droplet size distribution and surface area coverage during the measurements due to evaporation, coalescence, break off, and/or droplet motion. Acrylic was selected among other polymers because it is UV-curable and does not undergo any color change upon curing. It is also relatively viscous thus preventing the droplets from merging during deposition. The details of the sample preparation, droplet size distribution, and droplet contact angle measurements were reported in Ref. [38] and need not to be repeated.

Table 1
Summary of the acrylic droplet-covered glass samples used in this study [38].

Sample #	Surface treatment	Droplet contact angle $\bar{\theta}_c$ (°)	Projected diameter $\bar{d}_p \pm \sigma$ (μm)	Surface area coverage f_A (%)
1	None	25.8 ± 2.2	413 ± 194	40 ± 5
2	None	25.8 ± 2.2	614 ± 360	49 ± 5
3	None	25.8 ± 2.2	507 ± 283	59 ± 5
4	Rain-X®	37.1 ± 3.8	368 ± 740	45 ± 5
5	perfluorinated silane	54.8 ± 4.6	606 ± 323	52 ± 5
6	perfluorinated silane-treated silica nanoparticles	66.6 ± 4.5	250 ± 308	47 ± 5
7	50 nm Teflon film	76.2 ± 1.6	428 ± 143	19 ± 5
8	50 nm Teflon film	76.2 ± 1.6	271 ± 161	34 ± 5
9	50 nm Teflon film	76.2 ± 1.6	312 ± 193	45 ± 5

Table 1 summarizes the measured mean droplet contact angle $\bar{\theta}_c$, the mean projected diameter $\bar{d}_p$ plus or minus one standard deviation $\bar{d}_p \pm \sigma$, and the surface area coverage f_A of the samples used in this study. The mean droplet contact angle $\bar{\theta}_c$ and diameter $\bar{d}_p$ varied between 26° and 76° and 250 μm and 614 μm, respectively. The projected surface area coverage f_A varied between 19% and 60%.

2.2. Infrared sample characterization

The spectral normal-hemispherical transmittance $T_{nh,\lambda}$ and reflectance $R_{nh,\lambda}$ of the dry glass and glass slabs supporting droplets were measured using a nitrogen-purged Fourier transform infrared (FTIR) spectrometer (Nicolet^{TM} iS50, Thermo Scientific Fischer, USA) equipped with an integrating sphere (Upward IntegratIR^{TM}, PIKE Technologies, USA). A calcium fluoride (CaF$_2$) beamsplitter and an indium gallium arsenide (InGaAs) detector were used in the spectral range from 1.35 to 2.5 μm and a potassium bromide (KBr) beamsplitter and a liquid-nitrogen cooled mercury-cadmium-telluride (MCT) detector were used in the spectral range from 2 to 20 μm.

3. Analysis

3.1. Problem statement

Fig. 2 shows a schematic representation of a semitransparent glass window of thickness H and spectral complex index of refraction $m_{g,\lambda} = n_{g,\lambda} + i\,k_{g,\lambda}$, exposed to infrared radiation I_λ incident at an angle θ_i with wavelength λ. The glass window supported polydisperse spherical cap-shaped droplets with contact angle θ_c, projected diameter $d_p = d\cos\theta_c$ for $\theta_c \leq 90°$, and spectral complex index of refraction $m_{d,\lambda} = n_{d,\lambda} + i\,k_{d,\lambda}$ on either its (a) back side or (b) front side. For the back side configuration, the photons were first incident on the semitransparent glass slab where they could be reflected, absorbed, or transmitted. A fraction of the photons transmitted through the glass slab reached the absorbing droplets. These photons could be (i) absorbed by the droplets, (ii) internally reflected at the droplet/air interface, or (iii) transmitted through the droplet/air interface. For the front side configuration [Fig. 2(b)], the photons were directly incident on either the glass or the droplets. In either case, photons were reflected or refracted at each interface and could be absorbed by either the droplets or the glass slab. Here also, internal reflection may occur on the back surface of the glass window.

In order to rigorously validate our numerical code based on the MCRT method [31,46], the transmittance $T_{nh,\lambda}$ and reflectance $R_{nh,\lambda}$ of glass slabs supporting acrylic droplets were predicted using the precisely measured coordinates and projected diameters of all droplets deposited on the glass slab for (i) Sample 3 consisting of an uncoated glass slab covered with droplets with $\bar{\theta}_c = 25.8°$ and $f_A = 59\%$ and (ii) Sample 9 featuring a glass slab coated with a

(a) Back side
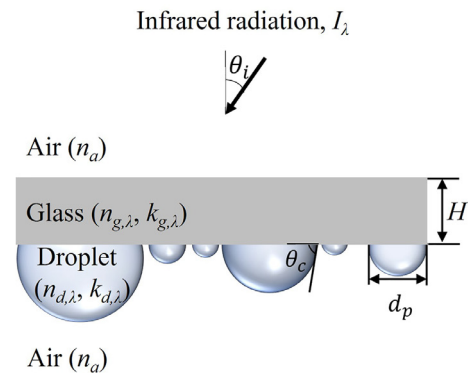
(b) Front side
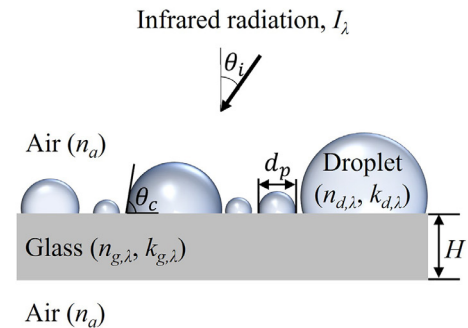
Fig. 2. Semitransparent glass window supporting absorbing polydisperse droplets on its (a) back side and (b) front side.

Teflon film with $\bar{\theta}_c = 76.2°$ and $f_A = 45\%$. Both back and front side configurations were simulated and compared with the experimental measurements in the infrared where both glass and acrylic are absorbing.

Once experimentally validated, the numerical code was used to predict the directional-hemispherical transmittance $T_{dh,\lambda}$ and reflectance $R_{dh,\lambda}$ of the glass windows supporting water droplets on their front or back sides. Here, the simulated water droplets were assumed to be spherical cap-shaped with the same coordinates (x, y) and projected diameters $d_p = d\cos\theta_c$ as the acrylic droplets deposited on Sample 3 with surface area coverage $f_A = 59\%$, in order to simulate a realistic droplet size distribution and surface area coverage f_A.

The underlying assumptions of the numerical code developed in Refs. [31,46] to predict numerically the transmittance $T_{dh,\lambda}$ and reflectance $R_{dh,\lambda}$ of the droplet-covered glass slabs were also used in this study and need not to be repeated.
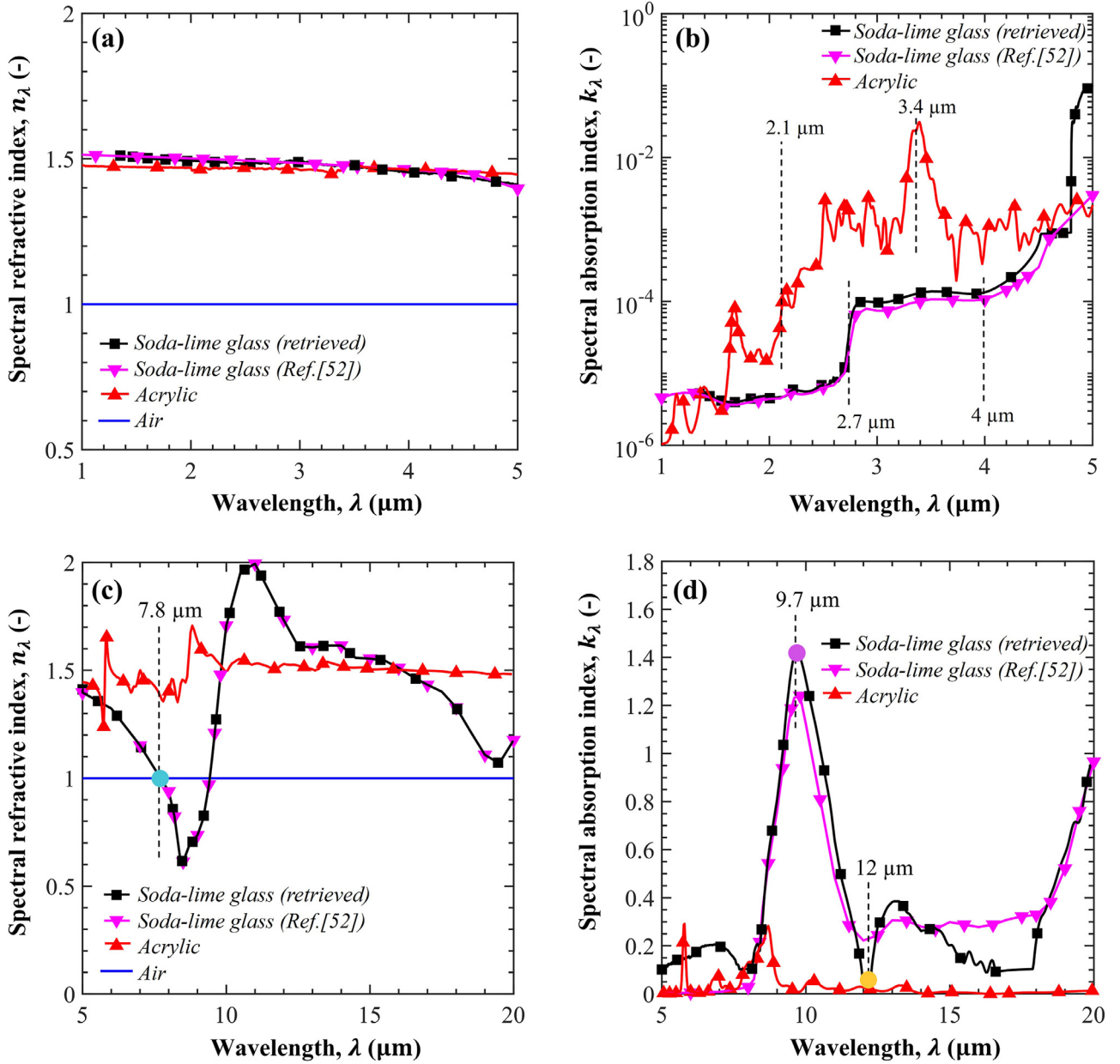
Fig. 3. Spectral refractive n_λ and absorption indices k_λ of glass slabs retrieved from measurements of $T_{nn,g,\lambda}$ and $R_{nn,g,\lambda}$ and those taken from Ref. [52] as well as those of acrylic in the spectral range between (a, b) 1.35 and 5 μm and (c, d) 5 and 20 μm.

### 3.2. Optical properties of soda-lime glass, acrylic, and water

The spectral refractive $n_{g,\lambda}$ and absorption $k_{g,\lambda}$ indices of the glass slab of thickness $H = 3$ mm were retrieved from the normal-normal transmittance $T_{nn,g,\lambda}$ and reflectance $R_{nn,g,\lambda}$ measurements in the spectral range from 1.35 to 20 μm by minimizing, for each wavelength, the sum δ_λ of the relative errors between the experimental measurements ($T_{nn,g,\lambda}$, $R_{nn,g,\lambda}$) and the theoretical predictions ($T^*_{nn,g,\lambda}$, $R^*_{nn,g,\lambda}$) for the transmittance and reflectance defined as

$$\delta_\lambda = \frac{\left| T_{nn,g,\lambda} - T^*_{nn,g,\lambda} \right|}{T_{nn,g,\lambda}} + \frac{\left| R_{nn,g,\lambda} - R^*_{nn,g,\lambda} \right|}{R_{nn,g,\lambda}}. \quad (1)$$

The pair ($n_{g,\lambda}$, $k_{g,\lambda}$) that minimized δ_λ was found using the sequential quadratic programming (SQP) method [48] ensuring that $\delta_\lambda < 5 \times 10^{-2}$. The analytical expressions for $T^*_{nn,g,\lambda}$ and $R^*_{nn,g,\lambda}$ can be found in Equation (2) in Ref. [38]. Fig. 3 shows $n_{g,\lambda}$ and $k_{g,\lambda}$

retrieved from the measured transmittance $T_{nn,g,\lambda}$ and reflectance $R_{nn,g,\lambda}$, of an uncoated glass slab between 1.35 and 20 μm. The spectral refractive $n_{d,\lambda}$ and absorption $k_{d,\lambda}$ indices of acrylic for the same wavelength range were also shown in Fig. 3, as reported in the literature [49–51]. The refractive and absorption indices of the air were taken as $n_a = 1.0$ and $k_a = 0$, respectively. As a reference, $n_{g,\lambda}$ and $k_{g,\lambda}$ of the clear soda-lime glass reported in Ref. [52] were also plotted. The retrieved refractive and absorption indices ($n_{g,\lambda}$, $k_{g,\lambda}$) of the glass window used in our study were in good agreement with those reported in the literature [52]. The slight difference can be attributed to the difference in the glass composition and in particular in the iron content [53].

Then, to predict the directional-hemispherical transmittance $T_{dh,\lambda}$ and reflectance $R_{dh,\lambda}$ of the glass windows supporting water droplets, the spectral refractive and absorption indices of the soda-lime silica glass and water were taken from Refs. [52] and [59], respectively.
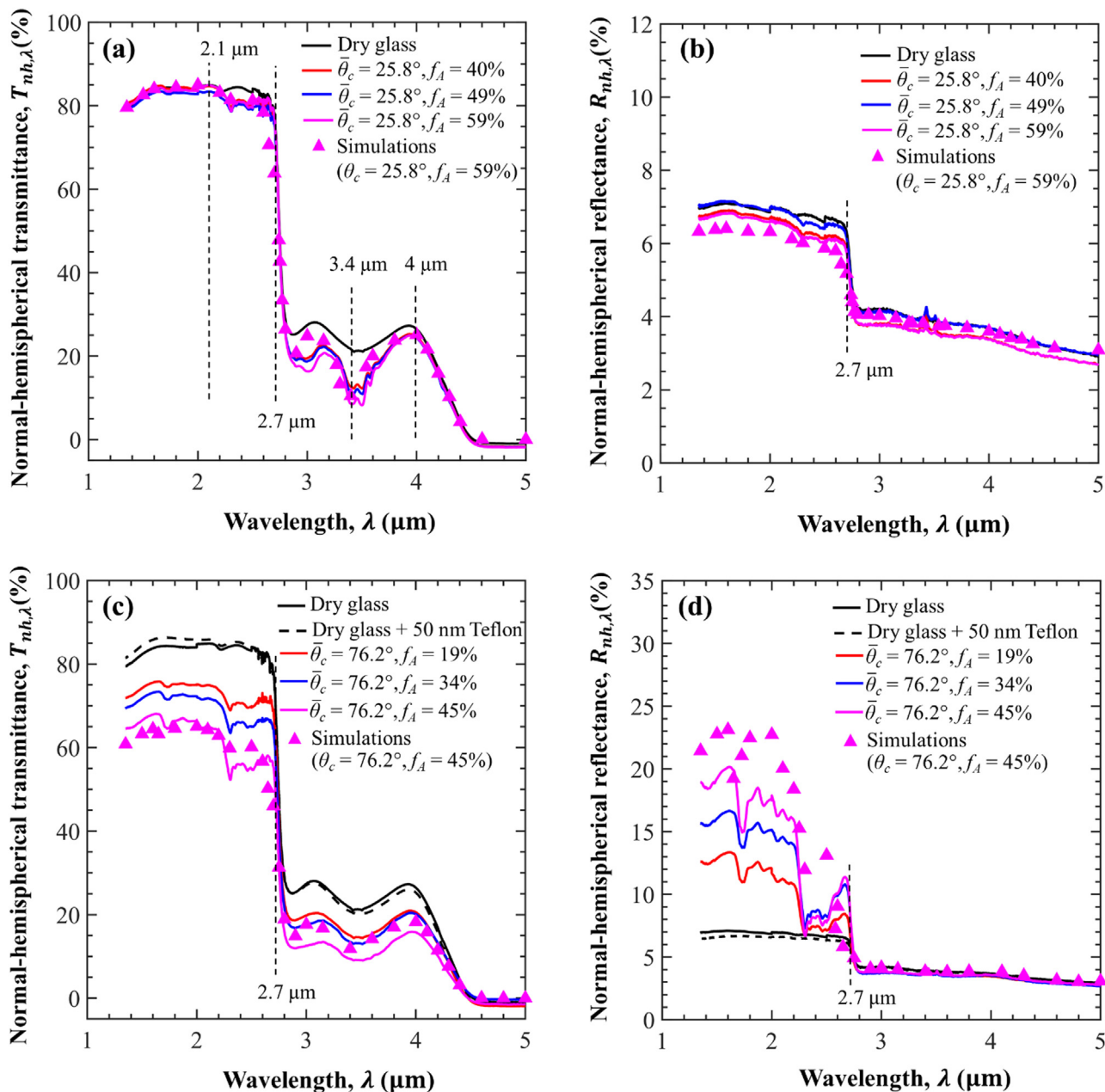
Fig. 4. Transmittance $T_{nh,\lambda}$ and reflectance $R_{nh,\lambda}$ as functions of wavelength λ for dry glass and glass slabs supporting droplets on their back side with (a, b) $\bar{\theta}_c = 25.8°$ and $f_A = 40$, 49, and 59% (Samples 1, 2, 3) and (c, d) $\bar{\theta}_c = 76.2°$ and $f_A = 19$, 34, and 45% (Samples 7, 8, 9).

3.3. Method of solution

The numerical predictions of the transmittance $T_{dh,\lambda}$ and reflectance $R_{dh,\lambda}$ of glass slabs covered with acrylic or water droplets on their back or front sides were obtained using the MCRT method described in detail in Refs. [31,46]. To ensure numerical convergence, 10^7 photon bundles for each numerical simulation were traced until they were counted as reflected, transmitted, or absorbed by the simulated sample.

4. Results and discussion

4.1. Back side condensation

4.1.1. Spectral normal-hemispherical transmittance and reflectance

Fig. 4 plots the spectral normal-hemispherical transmittance $T_{nh,\lambda}$ and reflectance $R_{nh,\lambda}$ measured between 1.35 and 5 μm for

glass slabs either dry or supporting acrylic droplets on their *back side* with (a, b) $\bar{\theta}_c = 25.8°$ and $f_A = 40$, 49, and 59% (Samples 1, 2, 3) and (c, d) $\bar{\theta}_c = 76.2°$ and $f_A = 19$, 34, and 45% (Samples 7, 8, 9). It is evident that the presence of droplets with low contact angle did not affect the transmittance $T_{nh,\lambda}$ for wavelengths $\lambda < 2.1$ μm when the droplet absorption index $k_{d,\lambda}$ was small [Fig. 3(b)]. These results corroborate the findings of previous analytical studies [32,34,46] which established that transmittance and reflectance are unaffected by the presence of pendant droplets when their contact angle θ_c is smaller than the critical angle for total internal reflection at the droplet/air interface defined as $\theta_{cr} = \sin^{-1}(n_a/n_d)$ $\approx 42.2°$ [54]. For the same reasons, Fig. 4(b) also shows that the reflectance $R_{nh,\lambda}$ was unaffected by droplets with $\bar{\theta}_c = 25.8°$ at all wavelengths. In fact, all droplet-covered samples had similar reflectance as the dry sample.

Furthermore, Fig. 4(a) indicates that the presence of droplets decreased the transmittance $T_{nh,\lambda}$ at wavelengths $\lambda = 2.1 - 4$ μm

for the different surface area coverages f_A considered. This was attributed to the absorption of the radiation by the droplets since the acrylic droplets were strongly absorbing in this spectral range, as shown in Fig. 3(b). In addition, the transmittance $T_{nh,\lambda}$ and reflectance $R_{nh,\lambda}$ of the dry and droplet-covered glass slabs decreased sharply at $\lambda = 2.7$ μm due to the sharp shoulder in $k_{g,\lambda}$ from 10^{-5} to 10^{-4} around 2.7 μm [Fig. 3(b)] corresponding to Si-OH stretching vibration [55]. Similarly, the transmittance $T_{nh,\lambda}$ of the droplet-covered glass slabs reached a local minimum at $\lambda = 3.4$ μm due to the peak in the absorption index of acrylic. However, for wavelengths $\lambda > 4$ μm, the presence of droplets did not change the transmittance $T_{nh,\lambda}$. This can be attributed to the fact that only a relatively small fraction of incident photons reached the back side of the glass slab due to its strong absorption index at $\lambda > 4$ μm. The few photons reaching the droplets did not experience backscattering due to the small droplet contact angle ($\bar{\theta}_c < \theta_{cr}$). In fact, the transmittance $T_{nh,\lambda}$ of all samples vanished for $\lambda \geq 4.8$ μm, as the glass absorption index $k_{g,\lambda}$ further increased. Fig. 4(a) and 4(b) also compare the numerically predicted and measured transmittance $T_{nh,\lambda}$ and reflectance $R_{nh,\lambda}$ of Sample 3 ($\bar{\theta}_c = 25.8°$, $f_A = 59\%$), respectively. They indicate that the numerical predictions were in good agreement with measurements of $T_{nh,\lambda}$ and $R_{nh,\lambda}$ across the entire spectral range considered. By contrast, Fig. 4(c) and 4(d) indicate that, for droplet contact angle $\bar{\theta}_c = 76.2°$, $T_{nh,\lambda}$ decreased and $R_{nh,\lambda}$ increased significantly with f_A for $\lambda < 2.7$ μm. This was attributed to total internal reflection at the droplet/air interface since the droplet contact angle was larger than the critical angle, i.e., $\bar{\theta}_c \geq \theta_{cr} \approx 42.2°$ and the glass did not absorb significantly ($k_{g,\lambda} \leq 10^{-5}$).

However, for $\lambda > 2.7$ μm, increasing the droplet surface area coverage f_A had a negligible effect on the reflectance $R_{nh,\lambda}$ while the transmittance $T_{nh,\lambda}$ still decreased with increasing f_A. This was due to the large absorption indices of glass $k_{g,\lambda}$ and acrylic $k_{d,\lambda}$ causing most photons to be absorbed by the glass window and those transmitted to be partially absorbed by the small droplets.

Moreover, Fig. 4(c) and 4(d) compare the simulated and measured transmittance $T_{nh,\lambda}$ and reflectance $R_{nh,\lambda}$ between 1.35 and 5 μm for Sample 9 ($\bar{\theta}_c = 76.2°$, $f_A = 45\%$), respectively. Both figures show relatively good agreement between measurements and numerical predictions. The discrepancies between the predicted and measured reflectance $R_{nh,\lambda}$ can be attributed to the fact that the MCRT simulations did not account for the Teflon film coating on the back side of the glass slab. In fact, Fig. 4 shows the measured (c) transmittance $T_{nh,g,\lambda}$ and (d) reflectance $R_{nh,g,\lambda}$ of glass slab with and without a 50 nm thick Teflon film. They indicate that $T_{nh,\lambda}$ of the glass slab slightly increased while $R_{nh,\lambda}$ decreased due to the presence of the Teflon film for wavelengths $\lambda < 2.7$ μm. Here, the Teflon film ($n \approx 1.29$) [56] reduced the refractive index mismatch at the glass/air interface ($n_g = 1.5$, $n_a = 1$) resulting in a decrease in the glass slab reflectance [38]. Thus, by ignoring the Teflon film, the MCRT simulations slightly overestimated the reflectance $R_{nh,\lambda}$ of Sample 9.

Fig. 5 plots the reflectance $R_{nh,\lambda}$ between 5 and 20 μm for the dry glass and glass slabs supporting droplets with (a) $\bar{\theta}_c = 25.8°$ and f_A between 40% and 60% (Samples 1-3) and (b) $\bar{\theta}_c = 76.2°$ and f_A between 19% and 45% (Samples 7-9). Note that the transmittance $T_{nh,\lambda}$ between 5 and 20 μm is not shown since it vanished for wavelengths $\lambda \geq 4.8$ μm beyond which the glass window was opaque ($k_{g,\lambda} \geq 10^{-3}$). First, Fig. 5(a) indicates that the reflectance of the dry glass $R_{nh,g,\lambda}$ initially decreased with increasing wavelength λ. $R_{nh,g,\lambda}$ reached zero at $\lambda = 7.8$ μm due to the absence of a refractive index mismatch at the glass/air interface, i.e., $n_{g,\lambda} = 1$ at $\lambda = 7.8$ μm, as illustrated by the blue dot in Fig. 3(c). In addition, the reflectance $R_{nh,g,\lambda}$ of the dry glass then reached a maximum at $\lambda = 9.7$ μm before decreasing to a minimum at $\lambda = 12$ μm re-
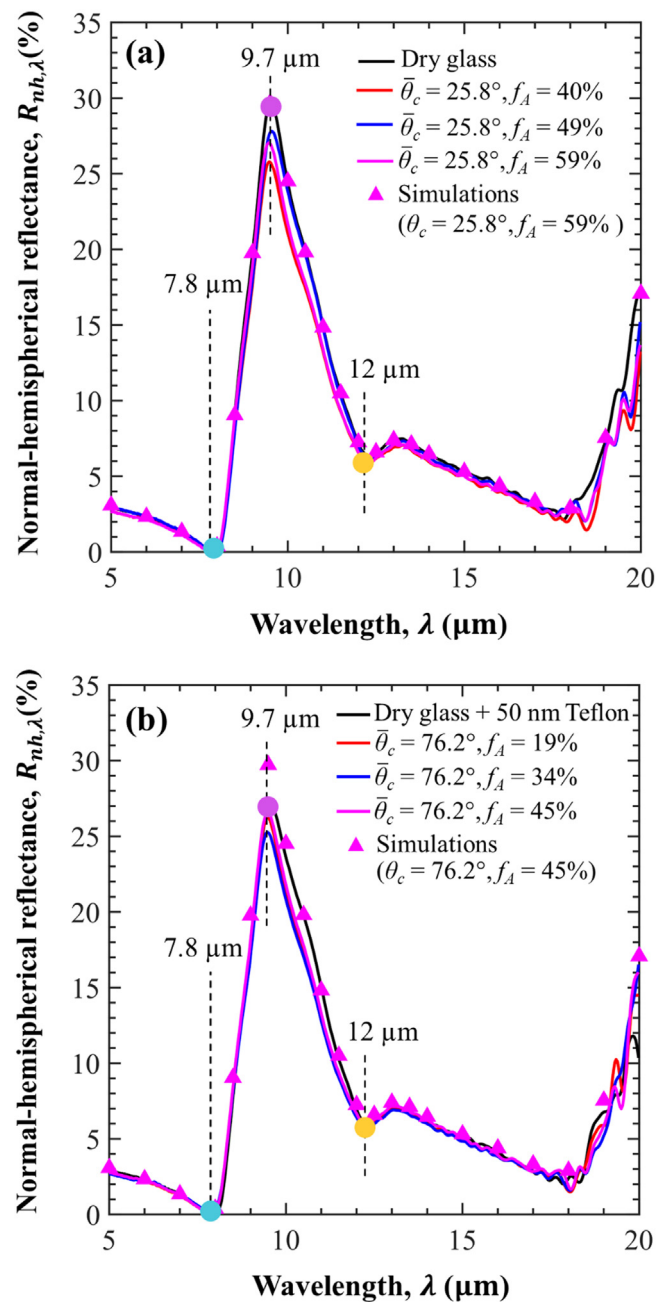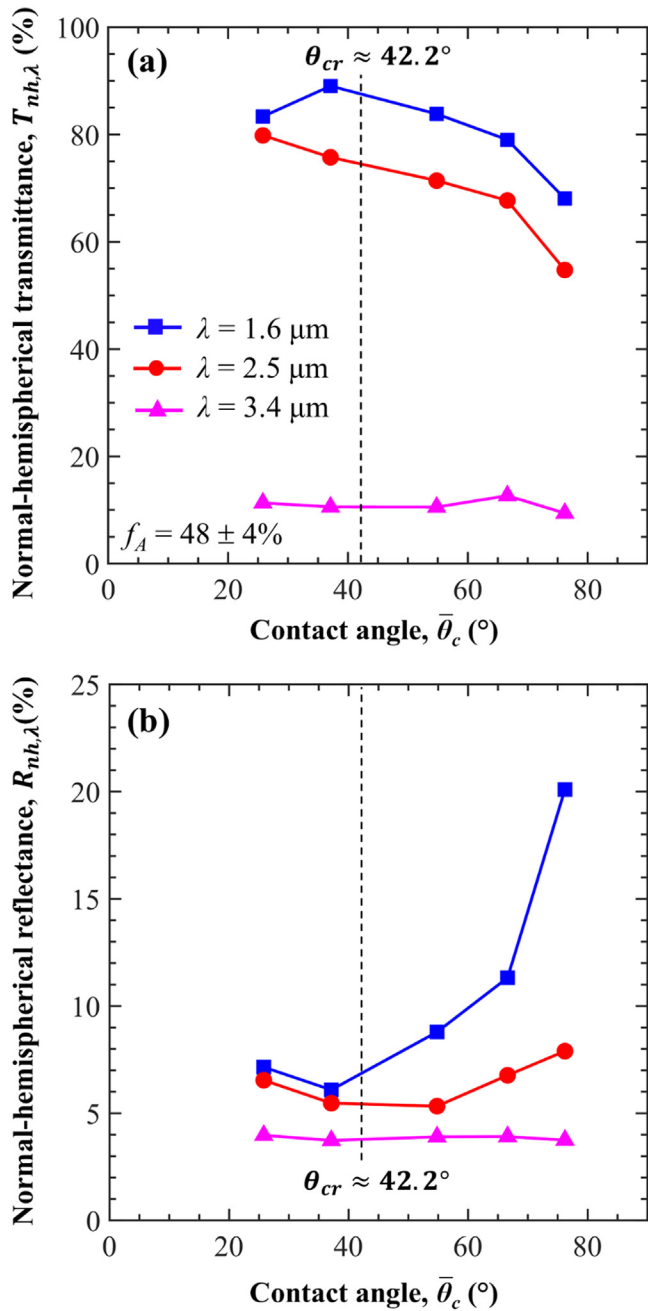

Fig. 5. Normal-hemispherical reflectance $R_{nh,\lambda}$ as a function of wavelength λ between 5 and 20 μm for dry glass and glass slabs supporting droplets on their back side with (a) $\bar{\theta}_c = 25.8°$ and $f_A = 40$, 49, and 59% (Samples 1, 2, 3) and (b) $\bar{\theta}_c = 76.2°$ and $f_A = 19$, 34, and 45% (Samples 7, 8, 9). In this wavelength range, $T_{nh,\lambda} = 0$.

spectively attributed to the peak at $\lambda = 9.7$ μm (purple dot) and subsequent trough at $\lambda = 12$ μm (yellow dot) in the spectral absorption index $k_{g,\lambda}$ of the glass slab [Fig. 3(d)].

Fig. 5 also indicates that, for wavelengths between 5 and 20 μm, the reflectance $R_{nh,\lambda}$ of the glass slabs supporting droplets was nearly independent of f_A regardless of the contact angle $\bar{\theta}_c$. Finally, the numerical simulations were in excellent agreement with the measurements for the dry and droplet-covered samples for both $\bar{\theta}_c = 25.8°$ and 76.2°.

4.1.2. Effect of droplet contact angle $\bar{\theta}_c$

Fig. 6 plots (a) the transmittance $T_{nh,\lambda}$ and (b) the reflectance $R_{nh,\lambda}$ as functions of $\bar{\theta}_c$ for glass slabs supporting droplets with f_A

Fig. 6. Normal-hemispherical (a) transmittance $T_{nh,\lambda}$ and (b) reflectance $R_{nh,\lambda}$ as functions of contact angle $\bar{\theta}_c$ for glass slabs supporting droplets with $f_A \approx 48 \pm 4\%$ (Samples 2, 4-6, 9) at wavelength $\lambda = 1.6$ ($k_{d,\lambda} = 10^{-5}$, $k_{g,\lambda} = 10^{-6}$), 2.5 ($k_{d,\lambda} = 10^{-3}$, $k_{g,\lambda} = 10^{-6}$), and 3.4 μm ($k_{d,\lambda} = 3 \times 10^{-2}$, $k_{g,\lambda} = 10^{-4}$).

$\approx 48 \pm 4\%$ (Samples 2, 4–9) at wavelength $\lambda = 1.6$, 2.5, and 3.4 μm. These wavelengths were selected to illustrate the effect of the absorption indices of the droplet and glass on the transmittance $T_{nh,\lambda}$ and reflectance $R_{nh,\lambda}$. The absorption index of the acrylic droplets $k_{d,\lambda}$ at wavelength $\lambda = 1.6$, 2.5, and 3.4 μm was equal to 10^{-5} (slightly absorbing), 10^{-3} (absorbing), and 3×10^{-2} (strongly absorbing) and that of the glass $k_{g,\lambda}$ was equal to 10^{-6}, 10^{-6}, and 10^{-4}, respectively. First, at wavelength $\lambda = 1.6$ μm, the transmittance $T_{nh,\lambda}$ increased while the reflectance decreased with increasing $\bar{\theta}_c$. This was due to the antireflecting effects of the slightly absorbing droplets reducing the index mismatch at the glass/air back surface. Second, the transmittance $T_{nh,\lambda}$ at wavelength $\lambda = 1.6$

μm decreased with increasing $\bar{\theta}_c$ for $\bar{\theta}_c > \theta_{cr}$ as the droplets were weakly absorbing. Simultaneously, the reflectance $R_{nh,\lambda}$ at wavelength $\lambda = 1.6$ μm increased. These observations can be attributed to total internal reflection occurring at the droplet/air interface, as discussed previously. Fig. 6(a) also indicates that the larger droplet absorption index $k_{d,\lambda}$ at $\lambda = 2.5$ μm caused the transmittance $T_{nh,\lambda}$ to decrease with increasing $\bar{\theta}_c$ even before reaching the critical angle θ_{cr}. On the other hand, the corresponding reflectance $R_{nh,\lambda}$ increased only slightly. This can be attributed to absorption by the droplets whose volume increased with increasing contact angle, as explained in Ref. [46]. Total internal reflection at the droplet/air interface also contributed to the increase in $R_{nh,\lambda}$ and the associated decrease in $T_{nh,\lambda}$ at $\lambda = 2.5$ μm for contact angles $\bar{\theta}_c > \theta_{cr}$. Finally, the transmittance $T_{nh,\lambda}$ and reflectance $R_{nh,\lambda}$ at $\lambda = 3.4$ μm of the droplet-covered glass slabs remained constant and independent of $\bar{\theta}_c$ when the glass window was strongly absorbing and only a small fraction of photons reached the droplets.

4.1.3. Effect of droplet surface area coverage f_A

Fig. 7 plots (a) the transmittance $T_{nh,\lambda}$ and (b) the reflectance $R_{nh,\lambda}$ as functions of f_A for the dry glass and glass slabs supporting droplets with $\bar{\theta}_c = 76.2°$ (Samples 7, 8, 9) at $\lambda = 1.6$, 2.5, and 3.4 μm. First, the transmittance $T_{nh,\lambda}$ decreased with increasing f_A at all wavelengths considered. This was attributed to total internal reflection at the droplet/air interface at $\lambda = 1.6$ μm and to absorption by the droplets and the glass slab at $\lambda = 3.4$ μm.

The steepest decrease in transmittance with increasing f_A was observed at $\lambda = 2.5$ μm as both total internal reflection and droplet absorption occurred. Moreover, Fig. 7(b) indicates that, at $\lambda = 1.6$ μm when droplets were weakly absorbing, the reflectance $R_{nh,\lambda}$ increased almost linearly with increasing f_A thanks to total internal reflection at the droplet/air interface. On the other hand, at $\lambda = 3.4$ μm when the glass was strongly absorbing, the reflectance $R_{nh,\lambda}$ remained constant and independence of f_A. At $\lambda = 2.5$ μm when the glass slab was weakly absorbing and the droplets slightly absorbing, $R_{nh,\lambda}$ remained constant and independent of f_A. This can be attributed to the fact that photons were absorbed by either the glass or the droplets after being refracted at the glass/air interface or backscattered at the droplet/air interface.

4.2. Front side condensation

4.2.1. Spectral normal-hemispherical transmittance and reflectance

Fig. 8 plots the transmittance $T_{nh,\lambda}$ and reflectance $R_{nh,\lambda}$ between 1.35 and 5 μm for the dry glass and glass slabs supporting droplets on their *front side* with (a, b) $\bar{\theta}_c = 25.8°$ and $f_A = 40\%$, 49%, and 59% (Samples 1, 2, 3) and (c, d) $\bar{\theta}_c = 76.2°$ and $f_A = 19$, 34, and 45% (Samples 7, 8, 9). For $\bar{\theta}_c = 25.8°$, the transmittance $T_{nh,\lambda}$ slightly increased while the reflectance $R_{nh,\lambda}$ decreased in the presence of droplets for $\lambda < 2.1$ μm. These trends were amplified for droplets with contact angle $\bar{\theta}_c = 76.2°$ [Fig. 8(c) and 8(d)]. These observations were due to the fact that droplets had an antireflection effect by reducing the refractive index mismatch at the air/droplet interface ($n_a = 1$, $n_d = 1.47$) compared to that at the air/glass interface ($n_a = 1$, $n_g = 1.51$). Moreover, Fig. 8(a) and 8(c) indicate that the transmittance $T_{nh,\lambda}$ decreased with increasing f_A for wavelengths between 2.1 and 4 μm due to absorption by the droplets for both contact angles considered, as explained in Ref. [31]. In fact, the transmittance $T_{nh,\lambda}$ featured ripples between 3.4 and 3.6 μm similar to those observed in the spectral absorption index $k_{d,\lambda}$ of acrylic plotted in Fig. 3(b).

Similarly, the Teflon film coating on the front side acted as an anti-reflective coating ($n \approx 1.29$). In fact, the presence of a 50 nm Teflon film on the dry glass window increased its transmittance and decreased its reflectance, particularly for $\lambda < 2.7$ μm. In addition, the increase in the transmittance $T_{nh,\lambda}$ for wavelengths $\lambda <$
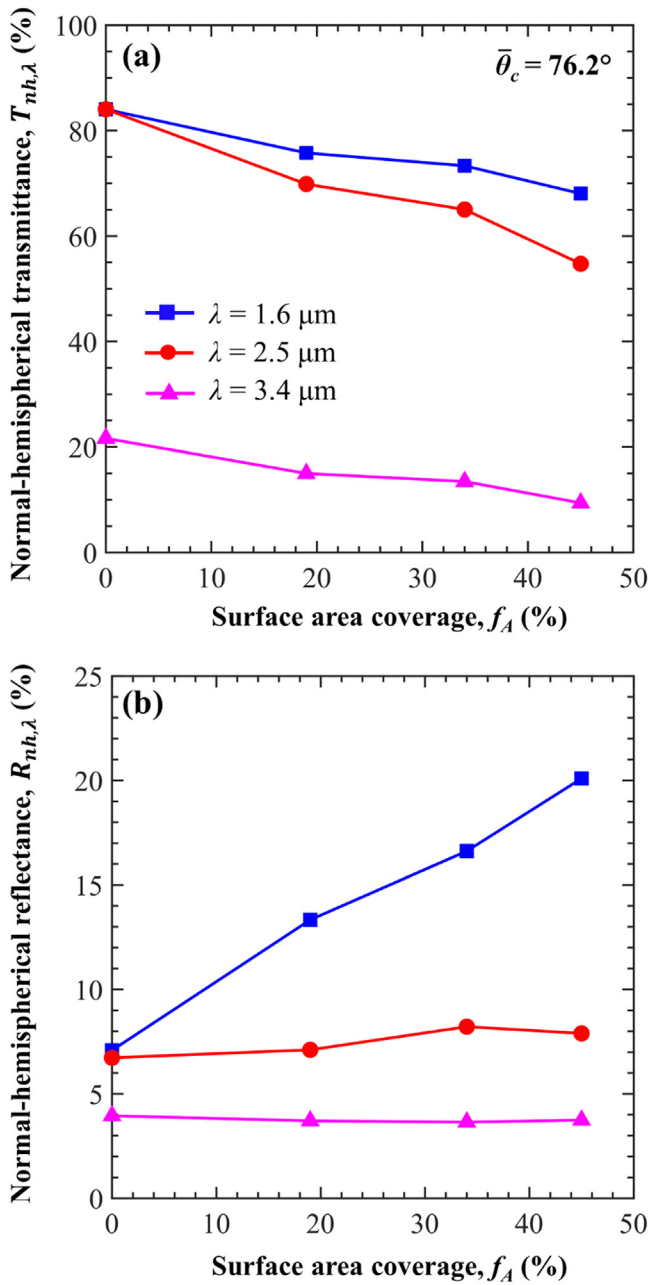
Fig. 7. Spectral normal-hemispherical (a) transmittance $T_{nh,\lambda}$ and (b) reflectance $R_{nh,\lambda}$ as functions of surface area coverage f_A for glass slabs supporting droplets on their back side with mean contact angle $\bar{\theta}_c = 76.2°$ (Samples 7, 8, 9) at $\lambda = 1.6$ ($k_{d,\lambda} = 10^{-5}$, $k_{g,\lambda} = 10^{-6}$), 2.5 ($k_{d,\lambda} = 10^{-3}$, $k_{g,\lambda} = 10^{-6}$), and 3.4 μm ($k_{d,\lambda} = 3 \times 10^{-2}$, $k_{g,\lambda} = 10^{-4}$).

2.1 μm was more pronounced for Samples 7-9 than for Samples 1-3 due to the presence of the Teflon film. Note that, for $\lambda > 2.7$ μm, $R_{nh,\lambda}$ remained nearly independent of f_A for $\bar{\theta}_c = 25.8°$ as shown in Fig. 8(b). It decreased only so slightly for $\bar{\theta}_c = 76.2°$ [Fig. 8(d)].

Finally, Fig. 8(a) and 8(b) establish that the numerical predictions were in very good agreement with the measurements of the transmittance $T_{nh,\lambda}$ and reflectance $R_{nh,\lambda}$ of Sample 3 ($\bar{\theta}_c = 25.8°$ and $f_A = 59\%$) across the IR spectrum considered. This further confirms the validity of the simulation tools for absorbing droplets present on the front side of a semitransparent window. Similarly, Fig. 8(c) and 8(d) compare numerical predictions and experimental measurements of the transmittance $T_{nh,\lambda}$ and reflectance $R_{nh,\lambda}$ for Sample 9 ($\bar{\theta}_c = 76.2°$ and $f_A = 45\%$), respectively. The measured

transmittance $T_{nh,\lambda}$ and reflectance $R_{nh,\lambda}$ were respectively larger and smaller than the numerical predictions for wavelengths $\lambda < 2.7$ μm. Here again, these discrepancies can be attributed to the presence of the Teflon coating.

Fig. 9 plots the reflectance $R_{nh,\lambda}$ between 5 and 20 μm for the dry glass and glass slabs supporting droplets on their front side featuring (a) $\bar{\theta}_c = 25.8°$ and f_A between 40% and 60% (Samples 1, 2, 3), and (b) $\bar{\theta}_c = 76.2°$ and f_A between 19% and 45% (Samples 7, 8, 9). Unlike for back side droplets (Fig. 5), the reflectance $R_{nh,\lambda}$ for front side droplets decreased significantly with increasing f_A for wavelengths between 8 and 15 μm due to the droplets antireflecting effect. In addition, $R_{nh,\lambda}$ for samples with droplet contact angle $\bar{\theta}_c = 76.2°$ further decreased due to the presence of the Teflon film and its additional antireflecting effect. Finally, Fig. 9 shows good agreements between measurements and numerical predictions of reflectance $R_{nh,\lambda}$.

4.3. Impact of water droplets on radiometric properties

To assess the impact of water droplets on the thermal load and radiometric properties of windows and covers used in buildings and solar energy conversion systems, the solar transmittance T_{sol} and the total hemispherical emittance ε of the dry and glass windows covered with cap-shaped water droplets on their front or back sides were predicted for a horizontal window exposed to direct and collimated solar radiation in Los Angeles, CA, USA (latitude: 34.07° N; longitude: 118.44° W) throughout the day on June 21st. First, the solar transmittance T_{sol} can be defined as [19,57]

$$T_{sol}(\theta_z(t)) = \frac{\int_{0.3\ \mu m}^{3\ \mu m} T_{dh,\lambda}(\theta_z(t))G_{sol,\lambda}(\theta_z(t))d\lambda}{\int_{0.3\ \mu m}^{3\ \mu m} G_{sol,\lambda}(\theta_z(t))d\lambda}. \tag{2}$$

Here, $\theta_z(t)$ is the time-dependent solar zenith, $T_{dh,\lambda}$ is the corresponding spectral directional-hemispherical transmittance, and $G_{sol,\lambda}$ is the spectral solar irradiation (in W/m$^2\cdot\mu$m) incident on a horizontal window for the location and day of interest taken from Ref. [58]. In order to evaluate $T_{sol}(\theta_z(t))$, the spectral directional-hemispherical transmittance $T_{dh,\lambda}$ was predicted numerically for water droplets using the previously experimentally-validated MCRT code in the visible [38] and infrared parts of the electromagnetic spectrum. The spectral range between 0.3 and 3 μm was considered because it accounts for 95% of the solar radiation. Fig. 10 plots the hourly solar transmittance T_{sol} calculated from the spectral directional-hemispherical transmittance $T_{dh,\lambda}(t)$ (see Supplementary Material) for dry and droplet-covered glass windows supporting water droplets on their (a) back side and (b) front side with droplet contact angle $\theta_c = 30°$, 60°, and 90°, and surface area coverage $f_A = 59\%$ on June 21st in Los Angeles, CA.

The solar transmittance of the glass windows decreased by up to 26% due to the presence of droplets on their back side for contact angles $\theta_c = 60°$ and 90° because of total internal reflection at the droplet/air interface and absorption by the water droplets. Note that, the solar transmittance T_{sol} remained unchanged between 11 AM and 3 PM in the presence of droplets with $\theta_c = 30°$. This can be explained by the fact that during this time, solar incident angles were near-normal ($\theta_i \leq 30°$) and the droplet contact angle θ_c was smaller than the critical angle $\theta_{cr} \approx 48.8°$ [54].

For glass windows supporting droplets on their front side, T_{sol} was divided by up to a factor 2 in the presence of water droplets due to the increase in reflection and absorption by the water droplets between 7 AM and 11 AM and from 3 PM to 7 PM. Here also, T_{sol} remained unchanged in the presence of water droplets between 11 AM and 3 PM due to the near-normal solar zenith angles ($\theta_z \leq 30°$). Note that in the early morning before 7 AM and evening after 7 PM when the solar radiation was incident at angles $\theta_z > 80°$, the glass windows supporting water droplets on
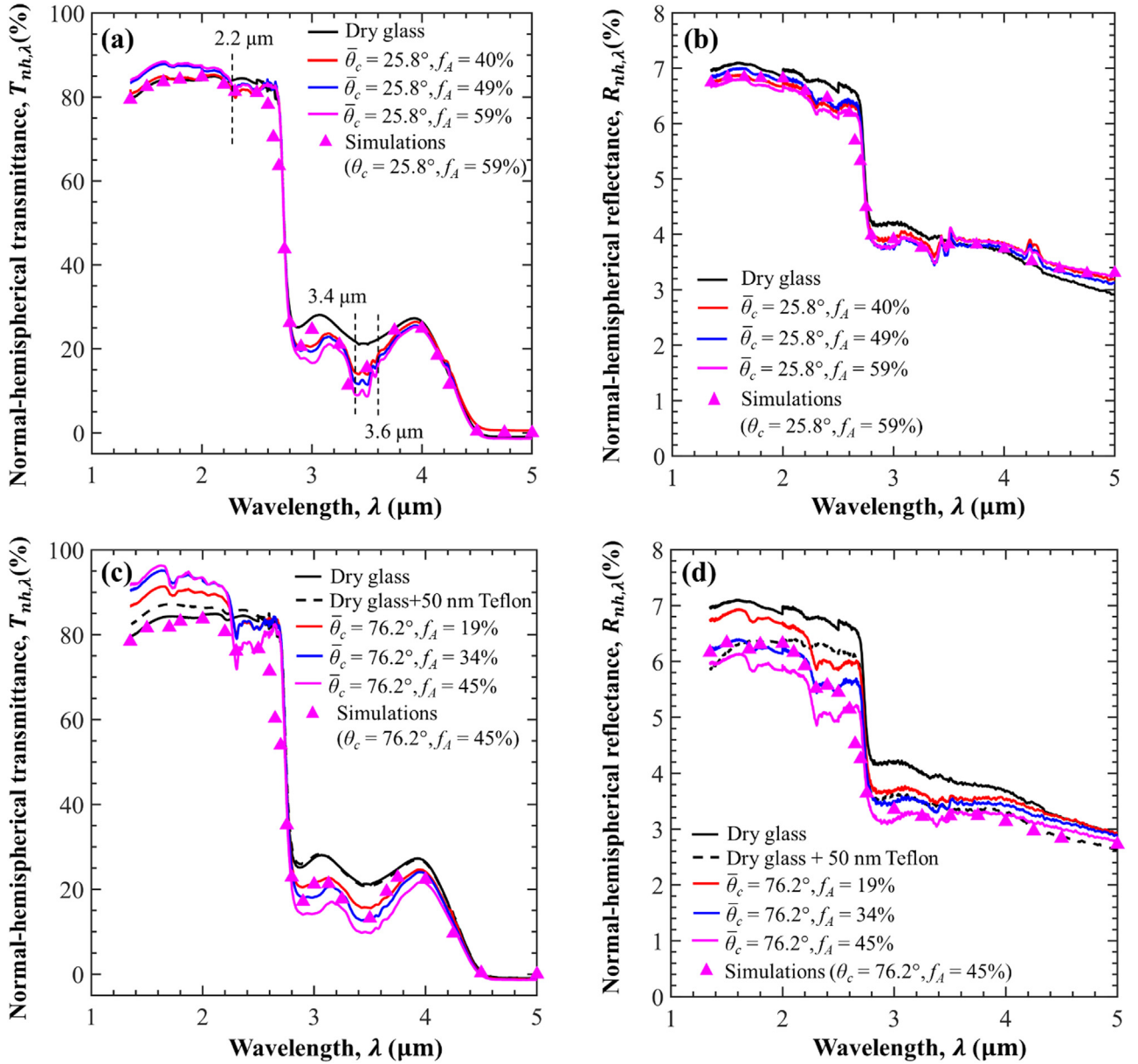
Fig. 8. Transmittance $T_{nh,\lambda}$ and reflectance $R_{nh,\lambda}$ as functions of wavelength λ for dry glass and glass slabs supporting droplets on their front side with (a, b) $\bar{\theta}_c = 25.8°$ and $f_A = 40$, 49, and 59% (Samples 1, 2, 3) and (c, d) $\bar{\theta}_c = 76.2°$ and $f_A = 19$, 34, and 45% (Samples 7, 8, 9).

their front side featured a larger solar transmittance T_{sol} than the dry glass window as the water droplets scattered the photons back towards the glass window [31]. Moreover, for $\theta_c = 90°$, the solar transmittance T_{sol} reached a minimum at 6:30 PM and then increased with increasing time until it reached a peak at 7:30 PM. This can be attributed to the decrease in total internal reflection at the back glass window/air interface and to the increase in total internal reflection at the water droplet/air interfaces [31,44].

Moreover, the above-mentioned systems operate at temperatures between 280 and 320 K and emit thermal radiation at infrared wavelengths that affects the thermal load on these systems. For an opaque medium, the spectral normal emittance $\varepsilon_{n,\lambda}$ given by Kirchhoff's law [19,62]

$$\varepsilon_{n,\lambda} = \alpha_{n,\lambda} = 1 - R_{nh,\lambda} \tag{3}$$

where $\alpha_{n,\lambda}$ is the spectral normal absorptance. The total hemispherical emittance ε does not differ considerably from the total normal emittance ε_n for dielectric materials [29], therefore ε can

be calculated as [19,29]

$$\varepsilon \approx \varepsilon_n = \frac{\int_{5\,\mu m}^{50\,\mu m} \varepsilon_{n,\lambda} E_{b,\lambda}(T_o)d\lambda}{\int_{5\,\mu m}^{50\,\mu m} E_{b,\lambda}(T_o)d\lambda}. \tag{4}$$

Here, $E_{b,\lambda}(T_o)$ is the blackbody spectral emissive power (in W/m^2·μm) at temperature $T_o = 296$ K. Note that the integrals in both the numerator and denominator of Equation (4) were truncated to wavelengths between 5 and 50 μm spectral range where 96% of their emissive power $E_{b,\lambda}(T_o)$ is concentrated and as the glass window was opaque for $\lambda \geq 4.8\ \mu$m. The validation of this approach is presented in Supplementary Material.

Fig. S3(c) in Supplementary Material shows the total hemispherical emittance ε [Equation (4)] as a function of droplet contact angle θ_c for water droplet-covered glass windows with surface area coverage $f_A = 59\%$. It indicates that the total hemispherical emittance ε of the glass window remained unchanged (see Fig. S3(a)) in the presence of water droplets on the back side. This was
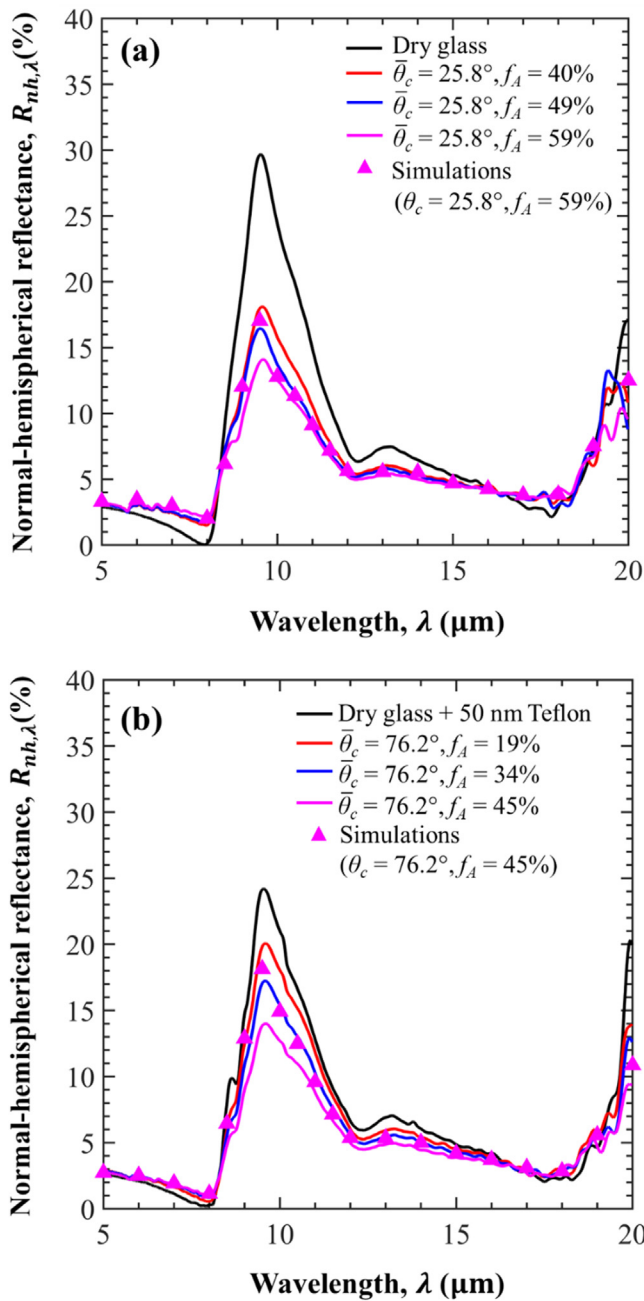
Fig. 9. Spectral normal-hemispherical reflectance $R_{nh,\lambda}$ as a function of wavelength λ for dry glass with and without Teflon coating and glass slabs supporting droplets on their front side with (a) $\bar{\theta}_c = 25.8°$ and $f_A = 40$, 49, and 59% (Samples 1, 2, 3) and (b) $\bar{\theta}_c = 76.2°$ and $f_A = 19$, 34, and 45% (Samples 7, 8, 9).

Fig. 10. Solar transmittance T_{sol} as a function of time t for a horizontal glass window supporting polydisperse water droplets on its (a) back and (b) front side for droplet contact angle $\theta_c = 30°$, 60°, and 90°, and surface area coverage $f_A = 59\%$ on June 21st, in Los Angeles, CA.

due to the fact that the glass window was strongly absorbing in this spectral range and photons did not reach the droplets. By contrast, ε increased slightly in the presence of water droplets on the front side from 0.93 for $f_A = 0\%$ to 0.96 for $f_A = 59\%$. This can be attributed to the (i) antireflecting effect and (ii) absorption of the IR radiation by the water droplets.

These results establish that the presence of water droplets on the back or front side of the glass windows can significantly reduce the solar transmittance T_{sol} at different times of the day and thereby the energy input and efficiency of solar energy conversion systems while their emittance remained nearly unchanged. In addition, hydrophilic coatings should be preferred to minimize the effect of droplets. However, note that most of the previous studies
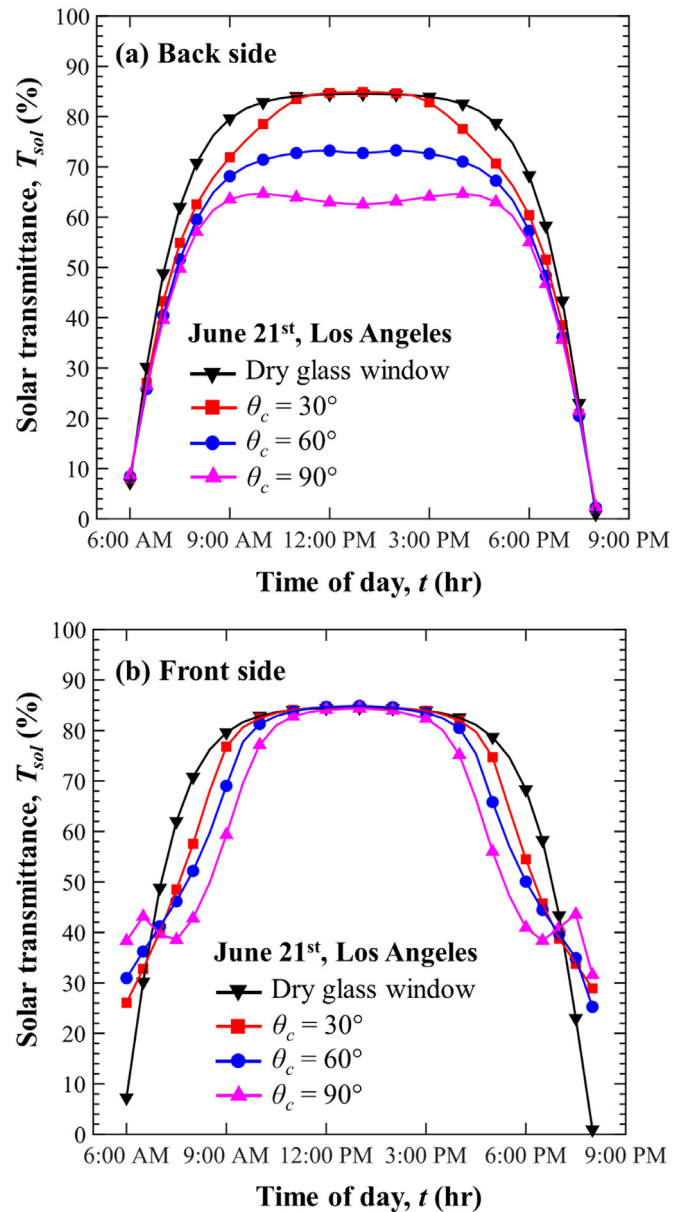
on the thermal modeling of solar energy conversion systems such as greenhouses [60] and solar stills [61] have not considered the presence of droplets and the hourly change in the solar transmittance of the cladding covered with droplets.

5. Conclusion

This study demonstrated that the radiation transfer through glass windows supporting droplets on their back side was controlled by absorption by the droplets and/or the glass window and by total internal reflection at the droplet/air interface. More specifically, when the droplets and the glass window were slightly absorbing, the transmittance $T_{nh,\lambda}$ was independent of droplet surface area coverage f_A and increased slightly with increasing droplet contact angle $\bar{\theta}_c$ for $\bar{\theta}_c < \theta_{cr}$. However, for $\bar{\theta}_c \geq \theta_{cr}$, the transmittance $T_{nh,\lambda}$ decreased with increasing contact angle $\bar{\theta}_c$ and surface area coverage f_A due to total internal reflection at the droplet/air inter-

face. Moreover, when the droplets were strongly absorbing and the glass was weakly absorbing, the transmittance $T_{nh,\lambda}$ decreased with increasing f_A and $\bar{\theta}_c$ due to absorption by both the droplets and glass. Finally, when the glass window was strongly absorbing, the transmittance $T_{nh,\lambda}$ vanished and the reflectance $R_{nh,\lambda}$ was independent of f_A and $\bar{\theta}_c$ as the radiation was reflected by the surface of the glass window and did not reach the droplets.

Radiation transfer through glass windows supporting droplets on their front side was affected by the antireflecting effects of droplets which reduced the index mismatch between the window and the air as well as by absorption by the droplets and/or the glass window. More specifically, when the droplets and the glass window were slightly absorbing, the transmittance $T_{nh,\lambda}$ increased while the reflectance $R_{nh,\lambda}$ decreased with increasing f_A. Moreover, when the droplets were strongly absorbing and the glass was weakly absorbing, the transmittance $T_{nh,\lambda}$ of glass windows supporting droplets on their front side decreased with increasing f_A and $\bar{\theta}_c$. Finally, when the glass window was strongly absorbing, the transmittance $T_{nh,\lambda}$ vanished and the reflectance $R_{nh,\lambda}$ decreased with increasing f_A.

The experimental results were successfully validated both qualitatively and quantitatively by predictions from numerical simulations based on Monte Carlo ray-tracing method [31,46] for both droplets on the back and front sides of glass windows. The experimentally-validated numerical simulation tool was used to predict the hourly solar transmittance and total hemispherical emittance of horizontal glass windows supporting cap-shaped water droplets on their back or front side in Los Angeles, CA on June 21. In the presence of droplets on the back side, the solar transmittance of the glass window decreased by up to 26% for most of the day while the total hemispherical emittance remained unchanged. However, for droplets on the front side, solar transmittance of glass window was divided by up to a factor 2 in the morning and evening while the total hemispherical emittance increased slightly. These results will be useful in selecting cover materials and surface coatings to improve and model solar energy conversion systems.

Declaration of Competing Interest

The authors declare that they have no known competing financial interests or personal relationships that could have appeared to influence the work reported in this paper.

CRediT authorship contribution statement

Eylul Simsek: Conceptualization, Methodology, Formal analysis, Investigation, Data curation, Visualization, Writing – original draft. **Megan J. Williams:** Formal analysis, Investigation, Data curation. **Jack Hoeniges:** Resources, Software, Validation. **Keyong Zhu:** Resources, Software, Validation. **Laurent Pilon:** Conceptualization, Methodology, Supervision, Project administration, Funding acquisition, Writing – review & editing.

Acknowledgment

Supplementary materials

Supplementary material associated with this article can be found, in the online version, at doi:10.1016/j.ijheatmasstransfer.2022.123043.

References

[1] L. Zuo, Y. Zheng, Z. Li, Y. Sha, Experimental investigation on the effect of cover material on the performance of solar still, in: Proceedings of the International Conference on Sustainable Power Generation and Supply (SUPERGEN), Hangzhou, China, 2012 September 8–9.

[2] R. Bhardwaj, M.V. ten Kortenaar, R.F. Mudde, Influence of condensation surface on solar distillation, Desalination 326 (2013) 37–45.

[3] G. Ni, S.H. Zandavi, S.M. Javid, S.V. Boriskina, T.A. Cooper, G. Chen, A salt-rejecting floating solar still for low-cost desalination, Energy Environ. Sci. 11 (6) (2018) 1510–1519.

[4] P. Zanganeh, A.S. Goharrizi, S. Ayatollahi, M. Feilizadeh, Productivity enhancement of solar stills by nano-coating of condensing surface, Desalination 454 (2019) 1–9.

[5] P. Zanganeh, A.S. Goharrizi, S. Ayatollahi, M. Feilizadeh, Nano-coated condensation surfaces enhanced the productivity of the single-slope solar still by changing the condensation mechanism, J. Clean. Prod. 265 (2020) 121758.

[6] V. Belessiotis, S. Kalogirou, E. Delyannis, Thermal Solar Desalination: Methods and Systems, 1st ed., Academic Press, London, UK, 2016.

[7] K.V. Modi, K.H. Nayi, Efficacy of forced condensation and forced evaporation with thermal energy storage material on square pyramid solar still, Renew. Energy 153 (2020) 1307–1319.

[8] J. Oshikiri, T.N. Anderson, Condensation control in glazed flat plate solar water heaters, in: Proceedings of the 23rd International Symposium on Transport Phenomena, Auckland, New Zealand, 2013 November 19–22.

[9] M.N. Nieuwoudt, E.H. Mathews, A mobile solar water heater for rural housing in Southern Africa, Build. Environ. 40 (9) (2005) 1217–1234.

[10] K. Ilse, B. Figgis, M.Z. Khan, V. Naumann, C. Hagendorf, Dew as a detrimental influencing factor for soiling of PV modules, IEEE J. Photovolt. 9 (1) (2019) 287–294.

[11] B. Figgis, A. Nouviaire, Y. Wubulikasimu, W. Javed, B. Guo, A. Ait-Mokhtar, R. Belarbi, S. Ahzi, Y. Remond, A. Ennaoui, Investigation of factors affecting condensation on soiled PV modules, Sol. Energy 159 (2018) 488–500.

[12] S.A. Hosseini, A.M. Kermani, A. Arabhosseini, Experimental study of the dew formation effect on the performance of photovoltaic modules, Renew. Energy 130 (2019) 352–359.

[13] C. Del Pero, N. Aste, F. Leonforte, The effect of rain on photovoltaic systems, Renew. Energy 179 (2021) 1803–1814.

[14] H.H. Al-Kayeim, M.A. Aurybi, S.I.U. Gilani, Influence of canopy condensate film on the performance of solar chimney power plant, Renew. Energy 136 (2019) 1012–1021.

[15] J.G. Pieters, M.J.J. Deltour, M.J.G. Debruyckere, Onset of condensation on the inner and outer surface of greenhouse covers during night, J. Agric. Eng. Res. 61 (1995) 165–171.

[16] I.V. Pollet, J.G. Pieters, Condensation and radiation transmittance of greenhouse cladding materials, part 1: laboratory measuring unit and performance, J. Agric. Eng. Res. 74 (1999) 369–377.

[17] I.V. Pollet, J.G. Pieters, Condensation and radiation transmittance of greenhouse cladding materials, part 2: results for a complete condensation cycle, J. Agric. Eng. Res. 75 (2000) 65–72.

[18] I.V. Pollet, J.G. Pieters, Condensation and radiation transmittance of greenhouse cladding materials, part 3: results for glass plates and plastic films, J. Agric. Eng. Res. 77 (2000) 419–428.

[19] G. Papadakis, D. Briassoulis, G. Scarascia Mugnozza, G. Vox, P. Feuilloley, J.A. Stoffers, Radiometric and thermal properties of, and testing methods for, greenhouse covering materials, J. Agric. Eng. Res. 77 (1) (2000) 7–38.

[20] F. Geoola, Y. Kashti, A. Levi, R. Brickman, Quality evaluation of anti-drop properties of greenhouse cladding materials, Polym. Test. 23 (7) (2004) 755–761.

[21] National Research Council Sustainable Development of Algal Biofuels in the United States, National Academies Press, Washington, DC, 2012.

[22] B.K. Behera, A. Varma, Microbial Resources for Sustainable Energy, Springer International Publishing, Cham, Switzerland, 2016.

[23] K.H. Mangi, Z. Larbi, J. Legrand, J. Pruvost, E.K. Si-Ahmed, Passive thermal regulation approach for Algofilm© photobioreactor through phase change, Chem. Eng. Res. Des. 168 (2021) 411–425.

[24] J. Hoeniges, K. Zhu, J. Pruvost, J. Legrand, E. Si-Ahmed, L. Pilon, Impact of dropwise condensation on the biomass production rate in covered raceway ponds, Energies 14 (2) (2021) 268.

[25] R. El Dlasty, I. Budaiwi, External condensation on windows, Constr. Build. Mater. 3 (2) (1989) 135–139.

[26] A. Werner, A. Roos, Condensation tests on glass samples for energy efficient windows, Sol. Energy Mater. Sol. Cells 91 (7) (2007) 609–615.

[27] A. Werner, A. Roos, Simulations of coatings to avoid external condensation on low U-value windows, Opt. Mater. 30 (6) (2008) 968–978.

[28] A. Laukkarinen, P. Kero, J. Vinha, Condensation at the exterior surface of windows, J. Build. Eng. 19 (2018) 592–601.

[29] T.L. Bergman, A.S. Lavine, F.P. Incropera, D.P. Dewitt, Fundamentals of Heat and Mass Transfer, 7th ed., John Wiley & Sons, Hoboken, NJ, 2011.

[30] B.J. Briscoe, K.P. Galvin, The effect of surface fog on the transmittance of light, Sol. Energy 46 (4) (1991) 191–197.

[31] K. Zhu, S. Li, L. Pilon, Light transfer through windows with external condensation, J. Quant. Spectrosc. Radiat. Transf. 208 (2018) 164–171.

[32] K. Zhu, Y. Huang, J. Pruvost, J. Legrand, L. Pilon, Transmittance of transparent windows with non-absorbing cap-shaped droplets condensed on their backside, J. Quant. Spectrosc. Radiat. Transf. 194 (2017) 98–107.

[33] J.G. Pieters, Interaction effects in simulating the light transmission through condensation drops on greenhouse covers, Trans. Am. Soc. Agric. Eng. 40 (5) (1997) 1463–1465.

[34] E.W. Tow, The antireflective potential of dropwise condensation, J. Opt. Soc. Am. A 31 (3) (2014) 493–499.

[35] I.V. Pollet, J.G. Pieters, Laboratory measurements of PAR transmittance of wet and dry greenhouse cladding materials, Agric. For. Meteorol. 93 (2) (1999) 149–152.

[36] I.V. Pollet, J.G. Pieters, PAR transmittances of dry and condensate covered glass and plastic greenhouse cladding, Agric. For. Meteorol. 110 (4) (2002) 285–298.

[37] J.G. Pieters, J.M. Deltour, M.J. Debruyckere, Light transmission through condensation on glass and polyethylene, Agric. For. Meteorol. 85 (1997) 51–62.

[38] E. Simsek, K. Zhu, G. N. Kashanchi, M. J. Williams, T. Galy, M. Marszewski, S. H. Tolbert, L. Pilon, Light transfer through semi-transparent glass panes supporting pendant droplets, J. Quant. Spectrosc. Radiat. Transf. 261 (2021) 107493.

[39] J. Hoeniges, K. Zhu, W. Welch, E. Simsek, L. Pilon, Transmittance of transparent horizontal and tilted windows supporting large non-absorbing pendant droplets, J. Quant. Spectrosc. Radiat. Transf. 275 (2021) 107876.

[40] B. Cemek, Y. Demir, Testing of the condensation characteristics and light transmissions of different plastic film covering materials, Polym. Test. 24 (2005) 284–289.

[41] F. Geoola, Y. Kashti, U.M. Peiper, Solar radiation transmissivity of greenhouse cladding materials, Acta Hortic. 534 (2000) 109–116.

[42] C. Stanghellini, M. Bruins, V. Mohammadkhani, G.J. Swinkels, P.J. Sonneveld, Effect of condensation on light transmission and energy budget of seven greenhouse cover materials, Acta Hortic. 952 (2012) 249–254.

[43] M.S. Ahamed, H. Guo, K. Tanino, Energy saving techniques for reducing the heating cost of conventional greenhouses, Biosystems Eng. 178 (2019) 9–33.

[44] E. Simsek, M.J. Williams, L. Pilon, Effect of dew and rain on photovoltaic solar cell performances, Sol. Energy Mater. Sol. Cells 222 (2021) 110908.

[45] Y. Huang, C. Feng, J. Hoeniges, K. Zhu, L. Pilon, Bidirectional transmittance of transparent windows with external or backside condensation of nonabsorbing cap-shaped droplets, J. Quant. Spectrosc. Radiat. Transf. 251 (2020) 107039.

[46] K. Zhu, L. Pilon, Transmittance of semitransparent windows with absorbing cap-shaped droplets condensed on their backside, J. Quant. Spectrosc. Radiat. Transf. 201 (2017) 53–63.

[47] C.K. Hsieh, A.K. Rajvanshi, The effect of dropwise condensation on glass properties, Sol. Energy 19 (1977) 389–393.

[48] J. Nocedal, S.J. Wright, Numerical Optimization, 2nd ed., Springer-Verlag, New York, NY, 2006.

[49] X. Zhang, J. Qiu, X. Li, J. Zhao, L. Liu, Complex refractive indices measurements of polymers in visible and near-infrared bands, Appl. Opt. 59 (8) (2020) 2337.

[50] X. Zhang, J. Qiu, J. Zhao, X. Li, L. Liu, Complex refractive indices measurements of polymers in infrared bands, J. Quant. Spectrosc. Radiat. Transf. 252 (2020) 107063.

[51] Hitachi High-technologies Corporation, "Measurement of optical characteristic of plastic by UH4150 spectrophotometer - an example of high throughput measurements" https://www.hitachi-hightech.com/products/images/12272/uh4150_data1_e.pdf (accessed April 15, 2021).

[52] M. Rubin, Optical properties of soda lime silica glasses, Sol. Energy Mater. 12 (4) (1985) 275–288.

[53] M.R. Vogt, H. Hahn, H. Holst, M. Winter, C. Schinke, M. Kontges, R. Brendel, P.P. Altermatt, Measurement of the optical constants of soda-lime glasses in dependence of iron content and modeling of iron-related power losses in crystalline Si solar cell modules, IEEE J. Photovolt. 6 (1) (2016) 111–118.

[54] J.R. Howell, R. Siegel, M.P. Mengüc, Thermal Radiation Heat Transfer, 5th ed., CRC Press, New York, NY, 2010.

[55] S.I. Amma, S.H. Kim, C.G. Pantano, Analysis of water and hydroxyl species in soda lime glass surfaces using attenuated total reflection (ATR)-IR spectroscopy, J. Am. Ceram. Soc. 99 (1) (2016) 128–134.

[56] R.A. Alawajji, G.K. Kannarpady, Z.A. Nima, N. Kelly, F. Watanabe, A.S. Biris, High temperature, transparent, superhydrophobic teflon AF-2400/indium tin oxide nanocomposite thin films, Nanotechnology 30 (17) (2019) 175702.

[57] G. Vox, E. Schettini, Evaluation of the radiometric properties of starch-based biodegradable films for crop protection, Polym. Test. 26 (5) (2007) 639–651.

[58] C. Gueymard, "Simple model of the atmospheric radiative transfer of sunshine (SMARTS). Version 2.9.5. 2005" https://www.nrel.gov/grid/solar-resource/smarts.html (accessed Aug. 10, 2021).

[59] G.M. Hale, M.R. Querry, Optical constants of water in the 200-nm to 200-μm wavelength region, Appl. Opt. 12 (3) (1973) 555.

[60] N. Choab, A. Allouhi, A. El Maakoul, T. Kousksou, S. Saadeddine, A. Jamil, Review on greenhouse microclimate and application: design parameters, thermal modeling and simulation, climate controlling technologies, Sol. Energy 191 (2019) 109–137.

[61] A. El-Sebaii, A.E.M. Khallaf, Mathematical modeling and experimental validation for square pyramid solar still, Environ. Sci. Pollut. Res. 27 (26) (2020) 32283–32295.

[62] S.A. Kalogirou, Solar Energy Engineering: Processes and Systems, 2nd ed., Academic Press, London, UK, 2014.